



Deep learning STEM-EDX tomography of nanocrystals

Yoseob Han^{1,5,6}, Jaeduck Jang^{1,6}, Eunju Cha^{1,6}, Junho Lee^{1,6}, Hyungjin Chung^{1,6}, Myoung-ho Jeong², Tae-Gon Kim³, Byeong Gyu Chae², Hee Goo Kim², Shinae Jun³, Sungwoo Hwang^{1,6}, Eunha Lee^{1,6} and Jong Chul Ye^{1,6}

Energy-dispersive X-ray spectroscopy (EDX) is often performed simultaneously with high-angle annular dark-field scanning transmission electron microscopy (STEM) for nanoscale physico-chemical analysis. However, high-quality STEM-EDX tomographic imaging is still challenging due to fundamental limitations such as sample degradation with prolonged scan time and the low probability of X-ray generation. To address this, we propose an unsupervised deep learning method for high-quality 3D EDX tomography of core-shell nanocrystals, which can be usually permanently damaged by prolonged electron beam. The proposed deep learning STEM-EDX tomography method was used to accurately reconstruct Au nanoparticles and InP/ZnSe/ZnS core-shell quantum dots, used in commercial display devices. Furthermore, the shape and thickness uniformity of the reconstructed ZnSe/ZnS shell closely correlates with optical properties of the quantum dots, such as quantum efficiency and chemical stability.

Semiconductor nanocrystals such as quantum dots (QDs)^{1,2} have been widely investigated thanks to their impressive size-dependent optoelectronic properties. Specifically, InP-based QDs are one of the most important materials in the display industry today. For example, InP/ZnSe/ZnS-QDs³ are Cd-free QDs, which are eco-friendly, with good optical properties and an optimized structure for commercial display. To improve performance, their core-shell structure must be characterized accurately, as shape and compositional distribution determine the material's photoelectronic characteristics and stability.

STEM has been widely applied to address this characterizational need, due to its capability of analysing structures at an atomic scale. In addition, it can often be simultaneously acquired with EDX for comprehensive elemental analysis of the sample⁴, as the incident accelerated electron beams used in STEM imaging cause the emission of characteristic X-rays from the atoms in the sample⁴. Unfortunately, QDs, with a size of several nanometres, are one of the most difficult materials to image with transmission electron microscopy (TEM), because the nanoparticles deform very easily under electron beams. Moreover, the image quality of an EDX map is severely limited by low signal collection efficiency and short acquisition time to avoid sample damage. Even in instances when the X-ray signals of nanoparticles can be measured for a prolonged period, it is difficult to obtain X-ray signals across the entire sample area. This is mainly because the EDX detector is only able to cover small solid angles (<10%), the probability of X-ray generation is low, and the geometry of a sample can limit the take-off angle of an X-ray photon and its collection efficiency (Fig. 1a).

The use of EDX tomography in studying 3D structures poses additional technical challenges. Tilting angles are limited by the sample holder, which in our experimental condition only allows the

sample to be tilted between -60° and $+60^\circ$ (Fig. 1). Moreover, to avoid specimen damage, a trade-off between the number of angular projections and the exposure time for each projection image is unavoidable. For example, in the experimental set-up shown in Fig. 1a, up to thirteen angular projections at 10° intervals were feasible without damaging the QD samples. Even with this limited number of projection views, all of the EDX projection images were extremely noisy (Fig. 2d). Under these conditions, analytical reconstruction algorithms such as filtered back-projection (FBP) cannot produce acceptable results from datasets containing these serious image artefacts. Research on EDX tomography^{5–8} has applied a simultaneous iterative reconstruction technique (SIRT)⁹, and exploited additional prior information including masks from annular dark-field STEM (ADF-STEM) reconstruction, to reduce streaking artefacts in sparse view reconstruction. However, the image quality offered by these methods is severely limited as shown in Fig. 2a.

To address this, we present a deep learning method for high-quality EDX 3D reconstruction. This is inspired by the recent success of deep learning for image reconstruction in X-ray CT (computed tomography)^{10–15}, MRI (magnetic resonance imaging)^{13,16–19}, positron emission tomography^{20,21}, ultrasound^{22,23}, optics^{24–26} and so on. Because one of the technical challenges in these inverse problems is ill-posedness, various regularization methods such as l_1 and total variation (TV)²⁷ have traditionally been exploited. Recent studies^{28,29} showed that the success of deep learning for image reconstruction originates from an intrinsic regularization effect, since a deep neural network can approximate a nonlinear mapping via a piecewise linear representation, providing a good architectural prior that can mitigate the ill-posedness. Furthermore, the number of piecewise regions, which determines the accuracy of the approximation by a deep neural network, increases exponentially with

¹Department of Bio and Brain Engineering, KAIST, Daejeon, Republic of Korea. ²Analytical Engineering Group, Samsung Advanced Institute of Technology, Samsung Electronics, Suwon-si, Gyeonggi-do, Republic of Korea. ³Inorganic Material Lab, Samsung Advanced Institute of Technology, Samsung Electronics, Suwon-si, Gyeonggi-do, Republic of Korea. ⁴Samsung Advanced Institute of Technology, Samsung Electronics, Suwon-si, Gyeonggi-do, Republic of Korea. ⁵Department of Radiology, Massachusetts General Hospital (MGH), Boston, MA, USA. ⁶These authors contributed equally: Yoseob Han, Jaeduck Jang, Eunju Cha, Junho Lee, Hyungjin Chung. [✉]e-mail: eunhayo.lee@samsung.com; jong.ye@kaist.ac.kr

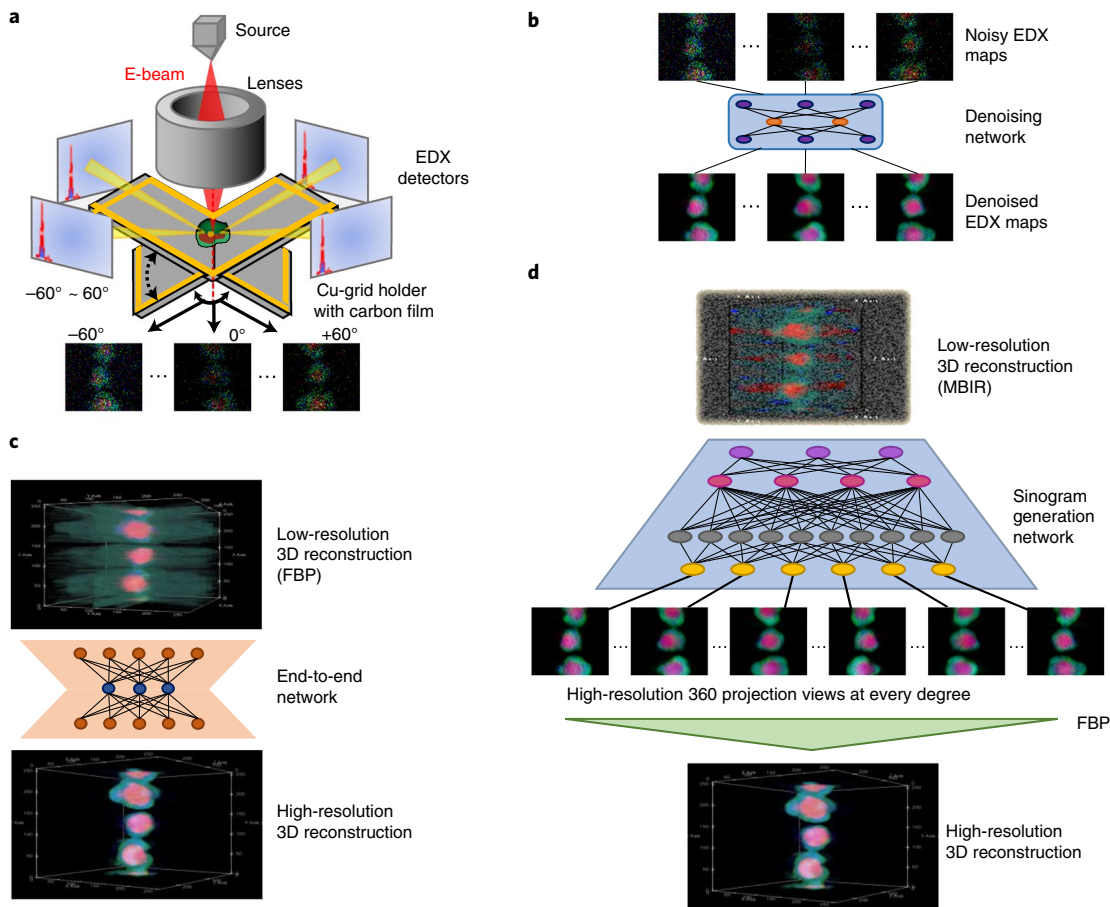


Fig. 1 | Deep learning STEM-EDX tomography workflow. **a**, The STEM-EDX system acquired a small number of raw EDX experimental maps within limited tilting angles. The rotating holder held the specimen and rotated its axis. EDX projection view data points and HAADF data were simultaneously acquired from -60 to 60° at 10° intervals. **b**, Our denoising network improves noisy EDX maps. This network is trained in an unsupervised manner. **c**, Our end-to-end learning network generates high-quality 3D reconstruction image directly from the noisy FBP reconstruction. This network is trained in a supervised manner using the inference image generated by **d**. **d**, In our unsupervised two-step network, a low-resolution 3D reconstruction is generated first using model-based iterative reconstruction. Then, a sinogram generation network produces EDX projection images across all angles, which are later used by FBP for high-resolution 3D reconstruction.

respect to the number of channels, depth and skipped connection, which makes the deep learning approach sufficiently accurate for inverse problems^{28,29}. Therefore, this study aims to develop a deep learning STEM-EDX tomography method for the 3D reconstruction of core-shell nanoparticles.

Unfortunately, a key technical challenge in applying deep learning for STEM-EDX tomography is that there exists no matched ground-truth label data that can be used for supervised training. Specifically, the existing deep learning approaches for image reconstruction are mainly based on the supervised learning framework that utilizes the matched pairs of measurement data and underlying images. While one could resort to simulation data for supervised training for imaging modalities with a known forward operator, such as Fourier transform in MRI and Radon transform for CT, the exact modelling of the measurement procedure in STEM-EDX tomography is extremely difficult due to characteristic X-ray photon generation, nonlinear detector physics and so on. In fact, deep learning reconstruction without the matched reference data is now of intense research interest in the machine learning and imaging community, but this field is still in the early phase of development. This is why there exists no deep learning approach for STEM-EDX tomography.

If we could obtain matched 3D reference data by some means, our neural network would be implemented in an end-to-end

manner (Fig. 1c), where the 3D noisy initial volume, which is reconstructed through FBP using the sparse projection views, is used as a deep neural network input so that the neural network can learn the mapping directly from the 3D noisy initial reconstruction to the matched high-quality 3D reference data. This makes the reconstruction process very simple for practical use.

Unfortunately, such high-quality matched reference data are not available for STEM-EDX; one of the main contributions of this paper is an unsupervised deep learning method (Fig. 1d). In fact, this unsupervised deep network could be used by itself, or for generating high-quality reference data for supervised training (Fig. 1c). These two approaches will be both explored.

For unsupervised neural network training (Fig. 1d), we impose consistency on the projection measurement data so that a neural network can generate synthetic projection data that are consistent with the measurement. Specifically, as shown in Fig. 1d, our unsupervised neural network is composed of two steps: the first produces an intermediate noisy 3D reconstruction from noisy sparse view raw EDX projection data, followed by the second, which generates enhanced projection measurement from the intermediate noisy 3D reconstruction. In particular, at the second step, the projection data from the noisy 3D reconstruction is enhanced by a convolutional neural network (CNN), imposing the consistency that the generated

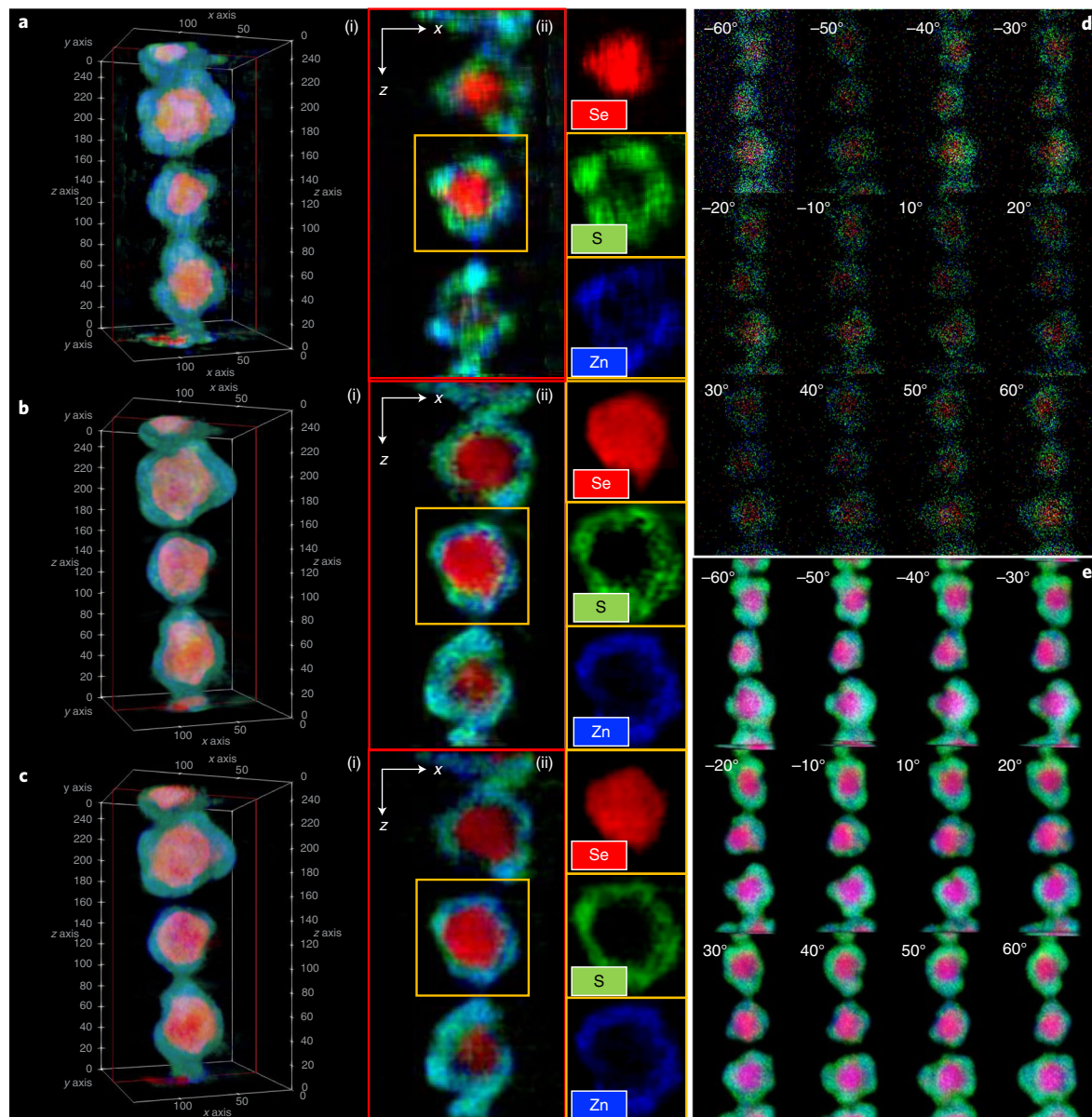


Fig. 2 | Commercially available QD reconstruction results. **a**, SIRT reconstruction results using spatial 11×11 average filtering to reduce measurement noise. 1 pixel = 2.68 \AA . **b**, Two-step network (Fig. 1d) reconstruction results. **c**, One-step end-to-end network (Fig. 1b) reconstruction results. (i) 3D rendering results. (ii) xz-plane cut-view images (the yellow box illustrates the magnified images for selenium (Se), sulfur (S) and zinc (Zn)). **d**, Examples of noisy EDX maps acquired by an EDX system. **e**, Denoised results from our unsupervised denoising network (Fig. 1b).

synthetic projection data at the measured angle should match the measured projection data. Such trained neural networks can then generate high-spatial resolution 360° projection views, even for unmeasured projection views (for example, every 1° increment). Then, an FBP algorithm is applied to produce a high-quality reconstruction from the enhanced 360° projection views. The main advantage of this method is that the intermediate 3D reconstruction and the analytic forward projection operation do not need to be accurate, as the neural network is trained to improve the resulting projection data so that the final reconstruction can be improved. Moreover, only the measurement data are used as a self-consistency condition so that the neural network does not require any supervised training. Another important contribution of this work is again an unsupervised denoising network in Fig. 1b, which improves the noisy EDX maps without introducing image blurring.

A detailed description of the network architecture and training procedure for these unsupervised neural networks (Fig. 1b,d) and the resulting end-to-end network (Fig. 1c) is provided in Methods and Supplementary Information.

In the following results, we show that with our proposed unsupervised learning method, accurate 3D reconstruction of Au-nanoparticles and QDs is possible. Furthermore, we analyse the optical characteristics of the samples, which correlate highly with the composition obtained from our reconstructions. These results establish the feasibility of our method.

Results

In order to verify the performance of our method, we conducted experiments using Au-nanorods (Creative Diagnostics, NY, USA). The purpose of this Au-nanorod experiment is to confirm whether

Table 1 | FSC resolution quantifications of the 3D reconstruction of elemental components of various nanoparticles by the proposed method

Nanoparticles	cQD			sQD1			sQD2		
	Se	S	Zn	Se	S	Zn	Se	S	Zn
3D resolution (nm)	0.68	0.60	0.68	0.45	0.42	0.44	0.41	0.41	0.45
Pixel pitch (nm)	0.27			0.19			0.19		

cQD, commercial QDs.

the proposed method proceeds well without making artefacts during the reconstruction process. Because Au-nanorods are composed of only one component, the shapes can be accurately measured using STEM-HAADF (high-angle annular dark-field) imaging. More specifically, we obtained STEM-HAADF images and then reconstructed their 3D composition. We acquired 13 projection views and each view took 3 minutes. Then, 2D EDX images from the same samples were used to reconstruct 3D maps. These reconstructions were then compared with the 3D ground-truth reconstructed from the STEM-HAADF images. Since they are nanoparticles composed of only one element, the reconstructed 3D EDX image must be the same as the reconstructed 3D STEM-HAADF image. As shown in Extended Data Fig. 1, the proposed method provides superior reconstruction results in terms of accuracy of the shape and compositional distribution within the particles. Moreover, although the STEM-HAADF ground-truth result using the vendor built-in reconstruction algorithm retains a limited-view artefact as indicated by arrows in Extended Data Fig. 1, the proposed method for EDX significantly reduces the artefact.

Our proposed deep learning STEM-EDX tomography method was then verified using commercially available QDs with a CdSe core and ZnS shell structure. EDX experimental maps were obtained at 13 angular views in an imaging protocol optimized for the QDs that included a well-established pre-treatment process^{30,31}. Despite the raw experimental maps being very noisy (Fig. 2d), our deep learning denoising network in Fig. 1b produced high-quality experimental maps (Fig. 2e). The 3D reconstruction results using conventional SIRT^{5,6} and the proposed method are shown in Fig. 2a,b. Additionally, extensive comparison with SIRT, TV and l_1 regularization methods are provided in Extended Data Fig. 2. In the reconstruction results by conventional methods, S was not visible since it was buried beneath the Se, and artefact patterns obstructed observation of the Zn in the nanoparticles. In addition, the boundary of each nanoparticle was not visible. However, reconstruction using the proposed method clearly revealed Se, S and Zn in the expected regions, and their boundaries were accurately reconstructed (Fig. 2b and Extended Data Fig. 2d). We have also provided end-to-end learning reconstruction results (Fig. 2c). The reconstruction results clearly show that similar 3D reconstruction results can be robustly obtained, although the result is a bit blurry. The blurring in the supervised end-to-end learning may be due to the limited training data set in STEM-EDX experiments as reported in existing works^{10,12,14,15,18,19}. Accordingly, the results that are presented as ‘proposed’ hereafter are reconstruction results using the unsupervised neural networks.

To further demonstrate the abilities of our proposed method, two types of InP/ZnSe/ZnS QDs with different shell morphologies were compared. Both QDs share the same InP cores with ~2 nm diameters, however the ZnSe shell coating processes were varied. The first type of QD (sQD1) was produced by adding the Se source through three split injections with 20 min term during slow heating from 180 °C to 320 °C for 1 h. The ZnSe shell of the second QD (sQD2) was coated by injecting the same amount of Se-trioctylphosphine (Se-TOP) into the reactor including InP cores and Zn(OA)₂ precursors in one injection and the mixture was rapidly heated to 320 °C

for 15 min. The second shell, ZnS, was coated using the same conditions for both sQD1 and sQD2. Synthesis procedure details can be found in the Methods section. In short, the morphological difference was realised by only changing the coating process of the ZnSe shell. Thus, sQD1 and sQD2 were expected to have the same core, but different ZnSe/ZnS shell morphology due to the different growth conditions. The surface of InP cores are easily oxidized, specifically during shell coating due to the strong thermodynamic tendency of oxidation to InPO_x and the supply of water from ketonization of carboxylate ligands^{32,33}. The single injection of the Se precursor and rapid heating used in the production of sQD2 resulted in rapid initial coating of ZnSe on the InP surface. This reduced the potential for core oxidation in comparison with the slow injection and heating for sQD1. The different oxidation levels might affect to the uniformity of shell coating in sQD1 and sQD2.

Two-dimensional elemental distribution (Extended Data Fig. 3) and size distributions for two types of QD were measured using conventional STEM-EDX analysis and low-magnification STEM-HAADF imaging (Extended Data Fig. 4), respectively. The size distribution of sQD2 was clearly more concentrated around the average value. The difference is presumably that sQD2 has less varied shell thickness than sQD1, because the cores of the two QDs are the same. The absorption spectrum of sQD2 exhibited a sharper exciton peak at around 500 nm than sQD1, as well as around 430 nm and 390 nm (Extended Data Fig. 5c). This corresponded with a stronger photoluminescence excitation (PLE) peak at around 500 nm and trough at around 420 nm in the PL-PL map (Extended Data Fig. 5a,b). These prominent absorption features are indicative of more uniform shell coating in the InP cores of sQD2.

Despite the differences in optical properties of sQD1 and sQD2, the conventional 2D images from the average kernel revealed that it was only possible to determine the presence or absence of elements, and the differences in content were not clear (Extended Data Fig. 3). Similarly, the differences between two types of QD were not clear in the SIRT 3D reconstructions (Extended Data Fig. 6a,b). However, our proposed method successfully identified morphological imperfections in the QDs by accurately recovering the spatial distribution of elements in the ZnSe and ZnS shells (Fig. 3a,b). The sQD1 shells were observed to have grown in specific directions, and few vertices were formed (Fig. 3a). As expected from the fabrication process, the boundaries of Se in sQD1 were not strictly concentrated in the core region. The thickness of the S shell varied widely and exhibited some discontinuity (Fig. 3a). On the other hand, ZnS shells of sQD2 grew evenly due to the improved fabrication method used, and Fig. 3b reveals its superior homogeneous layer structure. The Se component was concentrated in the core region, while S was found in the shell to ensure uniform thickness and continuity (Fig. 3b).

In Fig. 3a(iv), b(iv), S distributions from the cartesian-to-polar coordinate transformation are shown to quantify the differences in the 3D structure of the QDs along the radial direction (specific procedure described in Supplementary Fig. 11). Since the elemental components of the QDs are not spherically symmetrical, the statistics along the 1D radial profile turned out significantly dependent upon the particle origin. On the other hand, polar coordinate representation shows the thickness along the radial direction at

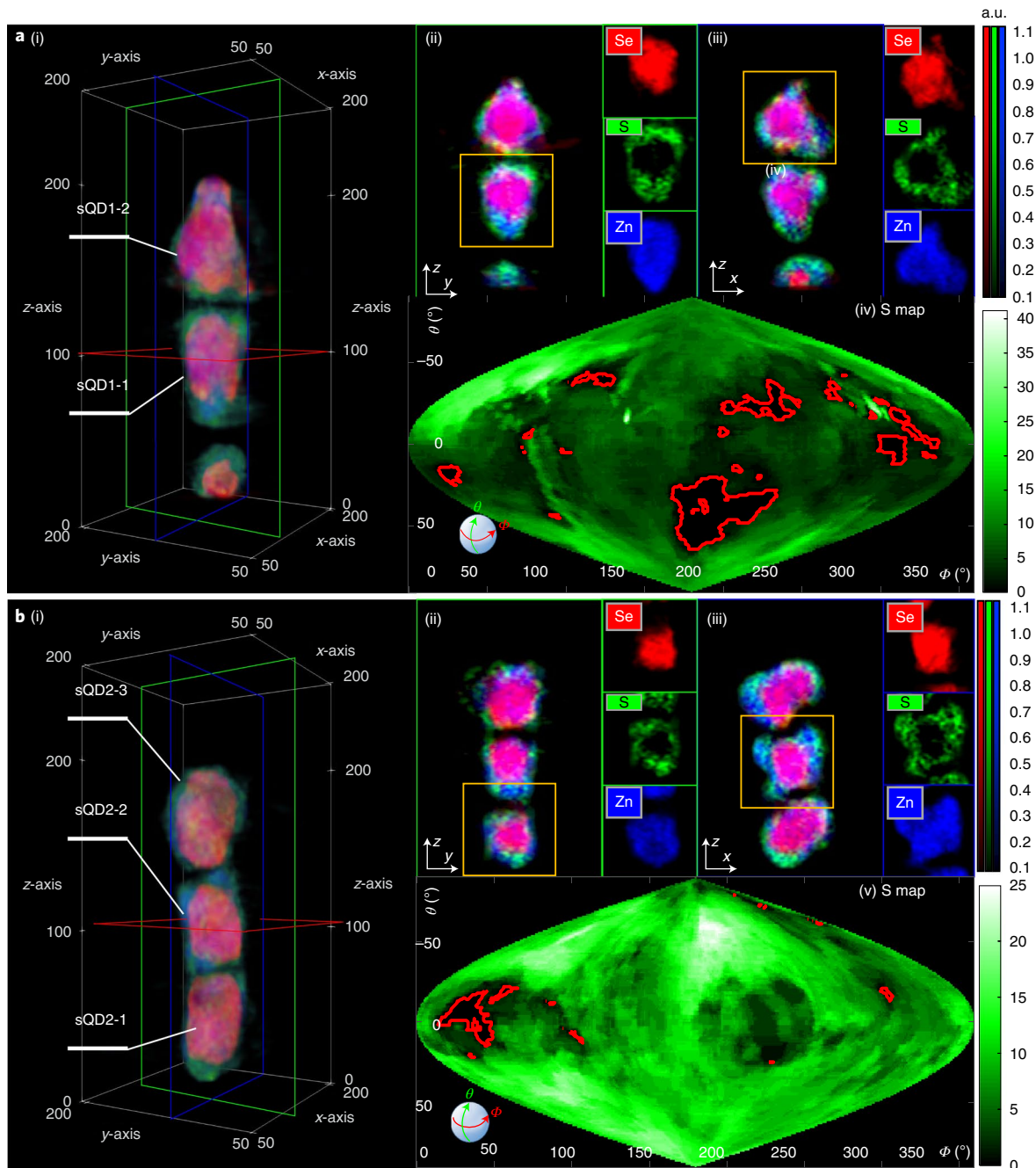


Fig. 3 | Proposed 3D STEM-EDX reconstruction results of two types of QDs. a,b, Reconstruction results using sQD1 (**a**) and sQD2. (**b**). (i)–(iii) 3D rendering results (1 pixel = 1.89 Å) (i); red, green and blue boxes indicate yz- (ii) and xz-plane (iii) cut-view images. (iv) Polar coordinate representation of S. The yellow box illustrates magnified images for selenium (Se), sulfur (S) and zinc (Zn).

(ϕ, θ) angular direction. Therefore, as long as the coordinate origin is inside the particle, the overall thickness distribution of our plot does not change except the specific coordinate in the polar plot, providing a robust way of presenting the information along the radial direction. The quantity of pixels containing each element along a fixed radius direction was evaluated to determine how evenly S surrounded the ZnSe. The polar coordinate representation of the 3D distribution of S revealed areas absent of S that were not identified using the conventional 2D image analysis (Fig. 3a(iv),b(iv)). The absence of S indicated areas in which the ZnS shell had not grown. The ZnS non-growth areas of sQD1-2 and sQD2-2 were 7.1% and 1.6%, respectively, as indicated by the

red lines in Fig. 3a(iv),b(iv). The non-growth of ZnS was associated with poor growth uniformity of the ZnSe shell, as uniform ZnSe shells did not have this issue (Extended Data Figs. 7–10). This indicates that the growth of ZnS was not only affected by external environmental conditions, but also the pre-existing morphology of the ZnSe shell. Lower incidence of ZnS non-growth region in sQD2 was observed due to the favourable synthesis conditions, and this was associated with a higher photoluminescent quantum yield (PL QY; $93 \pm 1\%$) than that of sQD1 ($87 \pm 1\%$). Thus, PL QY was closely related with the coating quality, since the uniform shell can effectively screen the interaction between the exciton lying around the InP cores and surface traps^{34,35}.

Table 2 | Nanoparticle specifications

Sample	Core–shell structure	Notes
sQD1, sQD2	InP (core); ZnSe (shell-1); ZnS (shell-2)	See Methods
Commercial QD	CdSe (core); ZnS (shell)	Ocean Nanotech, P/N QPP-665
Au nanoparticle	Pure Au	Commercial (Sigma Aldrich, P/N 752568)

When QDs are used in display devices as colour converting layers, QDs are fabricated as QD–polymer composites. However, PL QY is usually degraded when the QDs mixed with a polymer due to the detachment or forced rearrangement of ligands on the QD surfaces. Although both QD samples exhibited a decrease in PL QY after mixing with acrylate polymer, the 2% drop in sQD2 ($93 \pm 1\% \rightarrow 91 \pm 1\%$) was low in comparison with the 8% drop in sQD1 ($87 \pm 1\% \rightarrow 79 \pm 1\%$) (Extended Data Fig. 5d). The superior shell coating quality of sQD2 led to improved stability against external stress during device production. Therefore, the proposed deep learning reconstruction method confirms the 3D composition distribution and revealed that the absence of ZnS in specific areas affected the PL QY. This is believed to be an important advance over the conventional approaches that associate the optical characteristics with the overall shape uniformity due to the difficulty of obtaining 3D EDX reconstruction.

Finally, Table 1 quantifies the resolution of Se, S and Zn 3D reconstruction by the proposed method, which is computed using the Fourier shell correlation (FSC)³⁶. Although absolute resolution is difficult to measure due to the lack of the ground-truth, FSC is widely accepted for electron microscopy resolution quantification³⁶, and the relative resolution improvement can be seen with respect to the EDX raw data pixel pitch. The computed resolution confirmed that our reconstruction can resolve the elemental components of QDs. Moreover, given that the EDX raw data have pixel sizes of 268 pm (for commercial QD) and 189 pm (for sQD1 and sQD2), we can see that reconstruction resolution is about $2.2 \times$ (raw data pixel pitch), hence proportionally improved with better resolution EDX raw data.

Conclusion

In summary, nanocrystals such as QDs are difficult to accurately analyse using conventional STEM-EDX, but the 3D shape and compositional distribution are critical parameters to control their optical characteristics. Our proposed method using deep-learning STEM-EDX tomography enabled high-quality 3D reconstruction of the QDs that was sufficient for practical analysis. The analysis of Au-nanoparticles and various core–shell QD structures including InP/ZnSe/ZnS QDs showed that the proposed method produced high-quality 3D reconstructions that were highly correlated with the samples' optical characteristics. The accuracy of the method was thus confirmed, which demonstrated that STEM-EDX tomography can be used broadly for comprehensive physico-chemical analysis of nanoparticles.

Methods

TEM experiments. STEM-HAADF images and EDX elemental maps of various types of synthesized QDs, commercial QDs and commercial Au nanoparticles were used to train and test the neural network. Two transmission electron microscopes were used: FEI Titan cubed 60–300 and FEI Tecnai Osiris. Both were equipped with a Super-X EDX detector and high brightness X-FEG gun, of which the 80, 200 and 300 kV acceleration voltage modes were used. Data collection for EDX tomography was performed in a FEI Titan cubed 60–300 transmission electron microscope at 80 and 300 kV acceleration voltages. To avoid degradation of the sample by the electron beam, a low 80 kV acceleration voltage was applied to the synthesized sQD1 and sQD2. The 300 kV acceleration voltage was used for the commercial QD

and Au-nanoparticle samples, as they were more stable under the electron beam irradiation. The colloidal samples were dispersed on TEM grids with a carbon support film (Tedpella, P/N 01824) and mounted on a Fischerion-2020 tomography holder. A tilt series for the STEM-HAADF projection and EDX elemental map was acquired over a tilt range of -60° to $+60^\circ$ with in 10° increments using a screen current of 200 pA. At each angle, the element map with an image size of 256×256 pixels was recorded for 3 min for commercial QDs and 5 min for sQD1 and sQD2. The resulting EDX raw data have pixel sizes of 268 pm (for commercial QD) and 189 pm (for sQD1 and sQD2). The structure of nanoparticles are summarized in Table 2.

Materials. Indium acetate (In(OAc)_3 , 99.99%, Sigma-Aldrich), lauric acid (LA, 98%, Sigma-Aldrich), tris(trimethylsilyl)phosphine (TMS₃P, 98%, Strem), TOP (90%, Strem), 1-octadecene (ODE, 90%, Sigma-Aldrich), trioctylamine (TOA, 95%, Sigma-Aldrich), zinc acetate (99.99%, Sigma-Aldrich), oleic acid (OA, 90%, Sigma-Aldrich), sulfur (99.98%, Sigma-Aldrich), selenium (99.99%, Sigma-Aldrich), toluene (anhydrous, 99.8%, Sigma-Aldrich), ethanol (99.5%, Samchun Chemical), acetone (HPLC grade, Sigma-Aldrich), chloroform (HPLC grade, Sigma-Aldrich), oligomer (PO 94F, BASF), dipropylene glycol diacrylate (BASF), Irgacure Oxe01 (BASF), tetrahydromethylammonium hydroxide pentahydrate (TMAH-5H₂O, >97%, Sigma-Aldrich), and propylene glycol methyl ether acetate (PGMEA, >99.5%, Sigma-Aldrich) were used as purchased.

Synthesis of InP cores. An established synthetic method³⁰ was followed. Zinc acetate (1.2 mmol) and OA (2.4 mmol) were mixed in 10 ml of ODE in a reaction flask, and the mixture was evacuated at 120°C for 1 h, refilled with N₂ and cooled to room temperature. Indium acetate (0.6 mmol) and lauric acid (1.8 mmol) were added to the flask, placed under vacuum at 120°C for 1 h, and exchanged to N₂. The flask was heated to 150°C , a mixed solution of TMS₃P (0.4 mmol) and TOP (1 ml) was quickly injected and heated to 240°C . The reaction was monitored by measuring the absorption peak of the sampled aliquot. It was rapidly cooled to room temperature when an absorption peak was observed at around 430 nm. The resulting InP cores were centrifuged with acetone and re-dispersed in toluene for subsequent shell coating.

ZnSe/ZnS shell coating. An established synthetic method³⁰ was followed. Zinc acetate (8 mmol) and OA (16 mmol) were mixed with 10 ml of TOA to produce a Zn(OA)₂ precursor. The mixture was heated to 120°C under vacuum for 1 h and filled with N₂ gas. The mixture was heated to 180° to ensure that the Zn precursor was completely dissolved. The toluene solution containing the InP core QDs (~5 μm) was injected first, followed by 1.8 ml of 0.4 M Se/TOP. The sQD1 samples were formed by slowly heating the reaction mixture to 320°C for 1 h. The sQD2 samples were rapidly heated to 320°C over 15 min and held at the temperature for 45 min. To coat the ZnS shell, 2.4 ml of 1 M S/TOP solution was injected to the reaction flask, and the temperature was held at 320°C for 40 min. After cooling to 280°C , an additional 4.8 ml of 1.0 M S/TOP was injected and the mixture was left for 1 h. The final InP/ZnSe/ZnS QDs were centrifuged with ethanol and re-dispersed in toluene.

QD-acrylate composite. An established synthetic method³¹ was followed. Dried InP/ZnSe/ZnS QDs (0.3 g) were dispersed in 0.2 g of chloroform and mixed with 0.1 g of dispersants and 0.2 g of an oligomeric binder solution in 0.1 g of PGMEA for 15 min at room temperature. A mixture (300 mg) of PO 94F:dipropylene glycol diacrylate:Irgacure Oxe01:TiO₂:PGMEA (30 wt.%:15 wt.%:1.0 wt.%:5 wt.%:39 wt.%) mixture was added and blended for 30 min at room temperature in the dark. The photosensitive QD–polymer composition was spin-coated on a glass substrate to 5 μm thickness and pre-baked at 100°C for 2 min. The coated substrate was radiated by 365 nm UV light for 1 s. The substrate was heat-treated at 180°C in an oven under nitrogen for 30 min to produce a QD–polymer composite film.

Optical property characterization. UV-visible absorption spectra of the QDs were acquired using a UV spectrometer (Shimadzu UV-2600), and photoluminescence and photoluminescence excitation spectra were obtained using a fluorescence spectrophotometer (Hitachi F7000). Absolute PL QY of the QDs dispersed in toluene and QD–acrylate composite films were measured by placing the samples within the integrating half sphere of quantum efficiency measurement system (Otsuka QE-2100).

Resolution quantification using FSC. FSC³⁶ is a widely used criterion for estimating the resolution of 3D volume data x . By dividing the data x into an even particle volume x_{even} and an odd particle volume x_{odd} , the correlation is calculated in a series of concentric shells from two maps in the frequency domain. The Fourier shell index is given by:

$$\text{FSC}(k) = \frac{\sum_{|k_i|=r} F_{\text{even}}(k_i) \cdot F_{\text{odd}}^*(k_i)}{\sqrt{\sum_{k_i \in r} |F_{\text{even}}(k_i)|^2 \cdot \sum_{k_i \in r} |F_{\text{odd}}(k_i)|^2}}, \quad (1)$$

where F_{even} and F_{odd} denote the Fourier transform of x_{even} and x_{odd} , respectively; the asterisk (*) refers to the complex conjugate and $k_i \in \mathbb{R}^3$ denotes the k -space coordinate vector. Therefore, the $\text{FSC}(k)$ is represented as a function of the spatial

frequency, with the value at the origin being 1 and decreasing towards 0. The frequency that $\text{FSC}(k)$ first crosses the threshold value is used as a criterion for the resolution. Among various criteria such as 3σ criterion, 5σ criterion and 0.143 cut-off, we used 0.143 cut-off to obtain the resolution. To calculate the FSC-based resolution, we used an FSC server (<https://www.ebi.ac.uk/pdbe/emdb/validation/fsc/results/>) based on Imagic code provided by ImageScience Software.

Deep learning architecture. A linearized approximation of EDX forward measurement model can be described by equation (2):

$$y_\theta \simeq \mathcal{P}_\theta \circ \mathcal{R}x, \quad (2)$$

where x is the unknown 3D spectroscopic volume, y_θ is the collection of the EDX experimental maps measured at sparse set of angles Θ around the specimen rotation axis, \mathcal{R} is the X-ray transform to generate the 360 angular projection images at every 1° increment around the rotation axis, and \mathcal{P}_θ is the restriction to the set of finite projection angles Θ (see Fig. 1a for the experimental scenario and background).

Then, the goal of unsupervised training of the network in Fig. 1d is to impose the following consistency at the measured projection views:

$$\mathcal{Q}^D(y_\theta) \simeq \mathcal{Q}^S \circ \mathcal{P}_\theta \circ \mathcal{R} \circ \mathcal{M} \circ \mathcal{Q}^D(y_\theta) \quad (3)$$

where \mathcal{M} is a model-based iterative method (MBIR) to calculate an approximate 3D reconstruction and \circ denotes the composite function operator of two successive mappings. Here, \mathcal{Q}^D is the EDX experimental map denoising network (Fig. 1b) and \mathcal{Q}^S is the sinogram domain projection enhancement network. It is important to note that these two networks are trained in an unsupervised manner, since the training only requires the measurement dataset measured at sparse projection views by imposing the self-consistency in equation (3). Furthermore, the intermediate reconstruction from \mathcal{M} does not need to be high quality, since the projection enhancement network \mathcal{Q}^S will be trained to compensate for the blurry projection data. We also found that imposing the self-consistency after the projection image denoising network (\mathcal{Q}^D) is necessary, since it removes the noise from the EDX experimental map y_θ so that the self-consistency condition is less sensitive to the measurement noises. Once the two networks \mathcal{Q}^S and \mathcal{Q}^D are trained, then the synthetic high-resolution EDX projection data is generated at every 1° by

$$y_{360} = \mathcal{Q}^S \circ \mathcal{R} \circ \mathcal{M} \circ \mathcal{Q}^D(y_\theta) \quad (4)$$

after which the final high-spatial-resolution 3D reconstruction is obtained using

$$\hat{x} = \text{FBP}(y_{360}) \quad (5)$$

where FBP is the filtered backprojection algorithm using the 360 angular projection views. The detailed description of the training procedure is provided in the Supplementary Information.

For the single-step end-to-end neural network training in Fig. 1c, the aforementioned network is used to generate matched reference data. Then, from $\mathcal{Q}^D(y_\theta)$ we acquire an initial 3D volume through FBP. Subsequently, a 3D volume is reconstructed using an end-to-end neural network \mathcal{T} , which is trained in a supervised fashion with \hat{x} that was generated through the unsupervised learning scheme in equation (5). More specifically, the network is trained to match the following constraint:

$$\hat{x} = \mathcal{T}(\text{FBP}(\mathcal{Q}^D(y_\theta))). \quad (6)$$

Here, the end-to-end reconstruction network \mathcal{T} is a 3D convolutional neural network, which is adopted from the implementation of 3D U-Net³⁷, with a slight modification in normalization steps. Once the network is trained, 3D volume can be estimated directly through equation (6) without the model-based iterative reconstruction process, which greatly reduces the time of reconstruction.

Detailed descriptions of the training and inference procedures for these networks are provided in the Supplementary Information.

Data availability

The data acquired before and after processing, used to make figures in this paper are publicly shared in the same repository where our code is uploaded (<https://github.com/bispl-kaist/Deep-Learning-STEM-EDX-Tomography/> and <https://zenodo.org/record/4294003#.X8FjkBNKjOS>) under the directory 'Deep_Learning_STEM-EDX_Tomography/Recon_data'.

Code availability

The codes used in this study are available from <https://github.com/bispl-kaist/Deep-Learning-STEM-EDX-Tomography/> and <https://zenodo.org/record/4294003#.X8FjkBNKjOS>.

Received: 15 May 2020; Accepted: 22 December 2020;
Published online: 8 February 2021

References

- Alivisatos, A. P. Semiconductor clusters, nanocrystals, and quantum dots. *Science* **271**, 933–937 (1996).
- Loss, D. & DiVincenzo, D. P. Quantum computation with quantum dots. *Phys. Rev. A* **57**, 120 (1998).
- Won, Y.-H. et al. Highly efficient and stable InP/ZnSe/ZnS quantum dot light-emitting diodes. *Nature* **575**, 634–638 (2019).
- Goldstein, J. I. et al. *Scanning Electron Microscopy and X-ray Microanalysis* (Springer, 2017).
- Lepinay, K., Lorut, F., Pantel, R. & Epicier, T. Chemical 3D tomography of 28 nm high K metal gate transistor: STEM XEDS experimental method and results. *Micron* **47**, 43–49 (2013).
- Slater, T. J. et al. STEM-EDX tomography of bimetallic nanoparticles: a methodological investigation. *Ultramicroscopy* **162**, 61–73 (2016).
- Saghi, Z., Xu, X., Peng, Y., Inkson, B. & Möbus, G. Three-dimensional chemical analysis of tungsten probes by energy dispersive x-ray nanotomography. *Appl. Phys. Lett.* **91**, 251906 (2007).
- Zhong, Z., Goris, B., Schoenmakers, R., Bals, S. & Batenburg, K. J. A bimodal tomographic reconstruction technique combining EDS-STEM and HAADF-STEM. *Ultramicroscopy* **174**, 35–45 (2017).
- Gilbert, P. Iterative methods for the three-dimensional reconstruction of an object from projections. *J. Theor. Biol.* **36**, 105–117 (1972).
- Kang, E., Min, J. & Ye, J. C. A deep convolutional neural network using directional wavelets for low-dose X-ray CT reconstruction. *Med. Phys.* **44**, e360–e375 (2017).
- Chen, H. et al. Low-dose CT with a residual encoder-decoder convolutional neural network. *IEEE Trans. Med. Imaging* **36**, 2524–2535 (2017).
- Kang, E., Chang, W., Yoo, J. & Ye, J. C. Deep convolutional framelet denoising for low-dose CT via wavelet residual network. *IEEE Trans. Med. Imaging* **37**, 1358–1369 (2018).
- Jin, K. H., McCann, M. T., Froustey, E. & Unser, M. Deep convolutional neural network for inverse problems in imaging. *IEEE Trans. Image Process.* **26**, 4509–4522 (2017).
- Han, Y. & Ye, J. C. Framing U-Net via deep convolutional framelets: application to sparse-view CT. *IEEE Trans. Med. Imaging* **37**, 1418–1429 (2018).
- Han, Y., Kang, J. & Ye, J. C. Deep learning reconstruction for 9-view dual energy CT baggage scanner. In *Proc. Fifth International Conference on Image Formation in X-Ray Computed Tomography* 407–410 (CT Meeting, 2018).
- Wang, S. et al. Accelerating magnetic resonance imaging via deep learning. In *2016 IEEE 13th International Symposium on Biomedical Imaging* 514–517 (IEEE, 2016)..
- Hammernik, K. et al. Learning a variational network for reconstruction of accelerated MRI data. *Magn. Reson. Med.* **79**, 3055–3071 (2018).
- Lee, D., Yoo, J., Tak, S. & Ye, J. Deep residual learning for accelerated MRI using magnitude and phase networks. *IEEE Trans. Biomed. Eng.* **65**, 1985–1995 (2018).
- Han, Y. S., Yoo, J. & Ye, J. C. Deep learning with domain adaptation for accelerated projection reconstruction MR. *Magn. Reson. Med.* **80**, 1189–1205 (2018).
- Gong, K. et al. Iterative PET image reconstruction using convolutional neural network representation. *IEEE Trans. Med. Imaging* **38**, 675–685 (2018).
- Gong, K., Catana, C., Qi, J. & Li, Q. PET image reconstruction using deep image prior. *IEEE Trans. Med. Imaging* **38**, 1655–1665 (2018).
- Luchies, A. C. & Byram, B. C. Deep neural networks for ultrasound beamforming. *IEEE Trans. Med. Imaging* **37**, 2010–2021 (2018).
- Yoon, Y. H., Khan, S., Huh, J. & Ye, J. C. Efficient B-mode ultrasound image reconstruction from sub-sampled RF data using deep learning. *IEEE Trans. Med. Imaging* **38**, 325–336 (2019).
- Rivenson, Y. et al. Deep learning microscopy. *Optica* **4**, 1437–1443 (2017).
- Nehme, E., Weiss, L. E., Michaeli, T. & Shechtman, Y. Deep-STORM: super-resolution single-molecule microscopy by deep learning. *Optica* **5**, 458–464 (2018).
- Sinha, A., Lee, J., Li, S. & Barbastathis, G. Lensless computational imaging through deep learning. *Optica* **4**, 1117–1125 (2017).
- Donoho, D. L. Compressed sensing. *IEEE Trans. Inf. Theory* **52**, 1289–1306 (2006).
- Ye, J. C., Han, Y. & Cha, E. Deep convolutional framelets: a general deep learning framework for inverse problems. *SIAM J. Imag. Sci.* **11**, 991–1048 (2018).
- Ye, J. C. & Sung, W. K. Understanding geometry of encoder-decoder CNNs. In *Proc. 36th International Conference on Machine Learning* (eds Chaudhuri, K. & Salakhutdinov, R.) 7064–7073 (PMLR, 2019)..
- Kim, Y. et al. Bright and uniform green light emitting InP/ZnSe/ZnS quantum dots for wide color gamut displays. *ACS Appl. Nano Mater.* **2**, 1496–1504 (2019).
- Lee, S. & Lee, C. High-density quantum dots composites and its photolithographic patterning applications. *Polym. Adv. Technol.* **30**, 749–754 (2019).

32. Virieux, H. et al. InP/ZnS nanocrystals: coupling NMR and XPS for fine surface and interface description. *J. Am. Chem. Soc.* **134**, 19701–19708 (2012).
33. Stein, J. L. et al. Probing surface defects of InP quantum dots using phosphorus K α and K β X-ray emission spectroscopy. *Chem. Mater.* **30**, 6377–6388 (2018).
34. Hahm, D. et al. Design principle for bright, robust, and color-pure InP/ZnSe_xS_{1-x}/ZnS heterostructures. *Chem. Mater.* **31**, 3476–3484 (2019).
35. Reid, K. R., McBride, J. R., Freymeyer, N. J., Thal, L. B. & Rosenthal, S. J. Chemical structure, ensemble and single-particle spectroscopy of thick-shell inp–znse quantum dots. *Nano Lett.* **18**, 709–716 (2018).
36. Saxton, W. & Baumeister, W. The correlation averaging of a regularly arranged bacterial cell envelope protein. *J. Microsc.* **127**, 127–138 (1982).
37. Çiçek, Ö., Abdulkadir, A., Lienkamp, S. S., Brox, T. & Ronneberger, O. 3D U-Net: learning dense volumetric segmentation from sparse annotation. In *International Conference on Medical Image Computing and Computer-Assisted Intervention* 424–432 (Springer, 2016).

Acknowledgements

This research was supported by Samsung.

Author contributions

J.C.Y. and E.L. supervised the project in conception and discussion. J.J., E.L. and J.C.Y. co-conceived the project. Y.H., E.C. and H.C. performed experiments for 3D tomography reconstruction. T.-G.K. and S.J. prepared the SAIT QD samples. J.L. performed TEM

experiment and image reconstruction using SIRT. M.J., B.G.C. and H.G.K. performed TEM experiments. M.J. and J.J. performed image analysis. S.H. discussed the experiment and co-directed the project. Y.H., J.J., E.C., J.L., H.C., E.L. and J.C.Y. wrote manuscript.

Competing interests

Y.H., E.C., H.C. and J.C.Y. were supported by a research grant from Samsung Electronics. J.J., J.L., M.J., T.-G.K., B.G.C., H.G.K., S.J., S.H. and E.L. are employees of the Samsung Electronics. The authors declare no other competing interests.

Additional information

Extended data is available for this paper at <https://doi.org/10.1038/s42256-020-00289-5>.

Supplementary information The online version contains supplementary material available at <https://doi.org/10.1038/s42256-020-00289-5>.

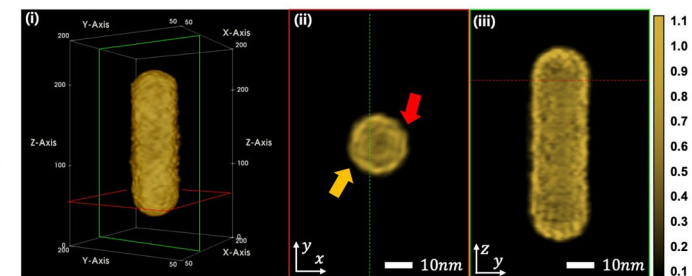
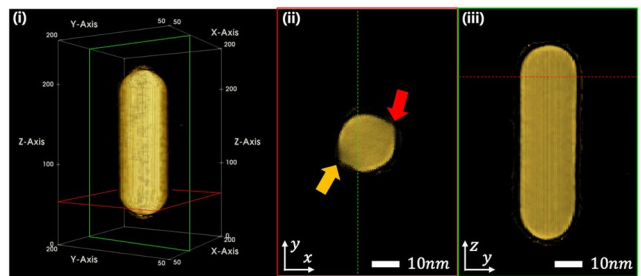
Correspondence and requests for materials should be addressed to E.L. or J.C.Y.

Peer review information *Nature Machine Intelligence* thanks the anonymous reviewers for their contribution to the peer review of this work.

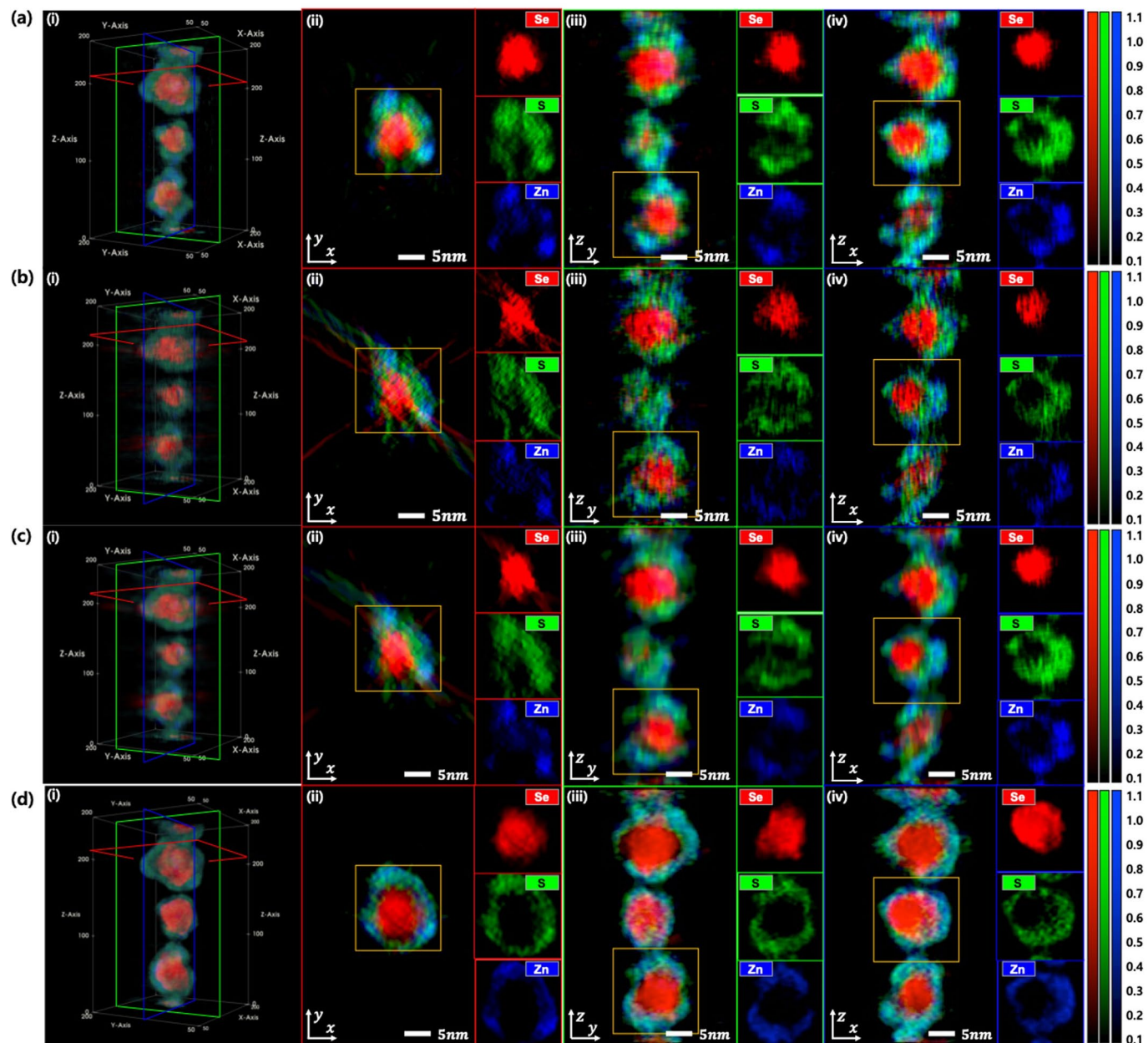
Reprints and permissions information is available at www.nature.com/reprints.

Publisher's note Springer Nature remains neutral with regard to jurisdictional claims in published maps and institutional affiliations.

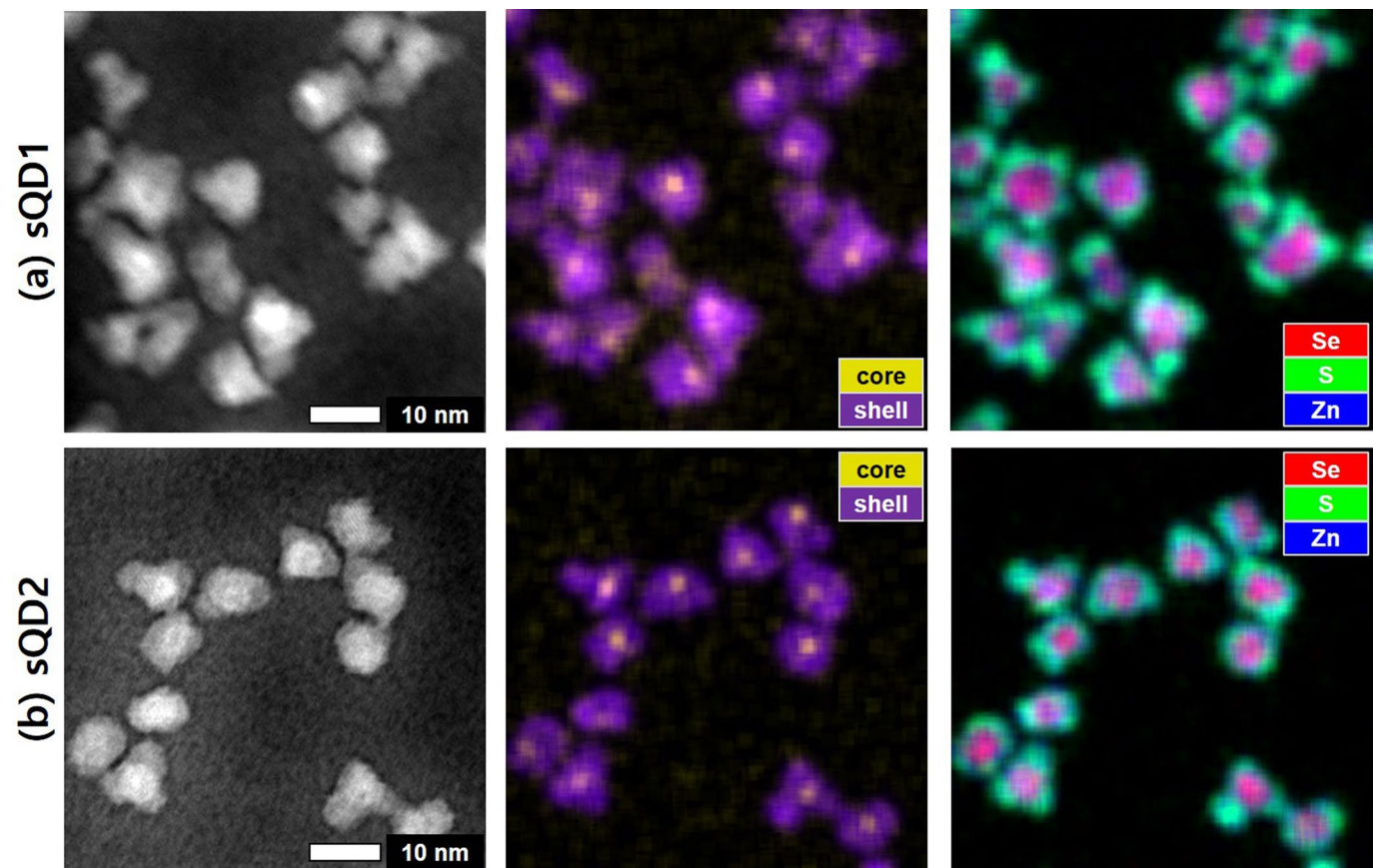
© The Author(s), under exclusive licence to Springer Nature Limited 2021



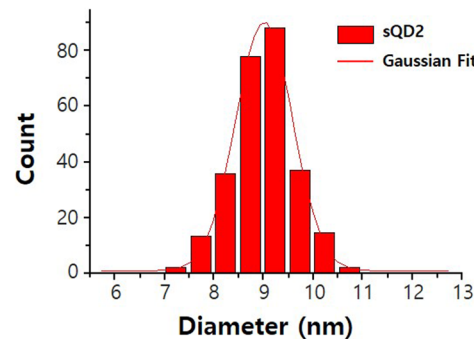
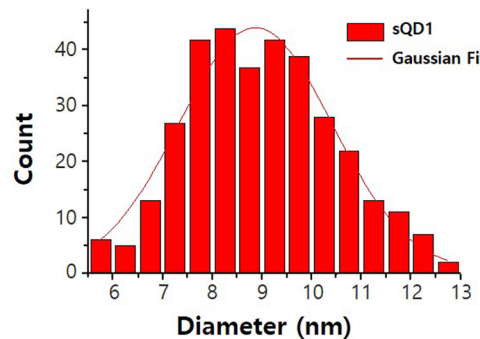
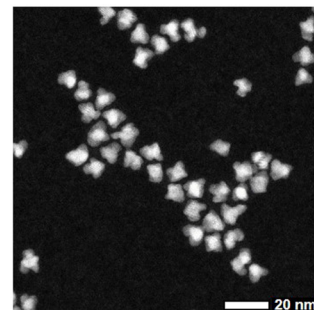
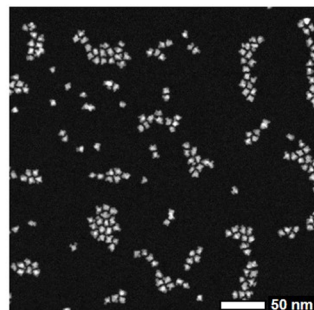
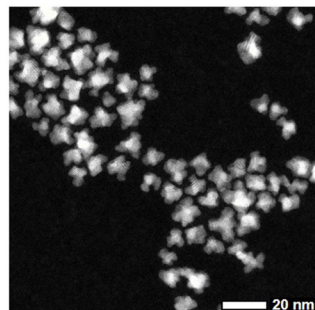
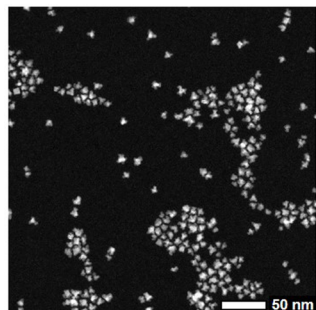
Extended Data Fig. 1 | 3D reconstruction results of Au-Nanorod for HAADF and EDX measurement. (a) HAADF ground-truth, and (b) proposed EDX reconstruction.



Extended Data Fig. 2 | Comparison of reconstructions using conventional methods and the proposed method. (a–c) Conventional reconstruction results for SIRT, L_1 regularization, and total variation (TV) penalty with spatial 11×11 average filter to reduce the measurement noises and (d) our reconstruction results of commercially available QDs. (i) shows the 3D rendering results, and red, green, and blue boxes in (i) indicate (ii) xy-, (iii) yz-, and (iv) xz-plane cut-view images, respectively. Yellow box illustrates the magnified images. Se, S, and Zn refer selenium, sulphur, and zinc components, respectively.



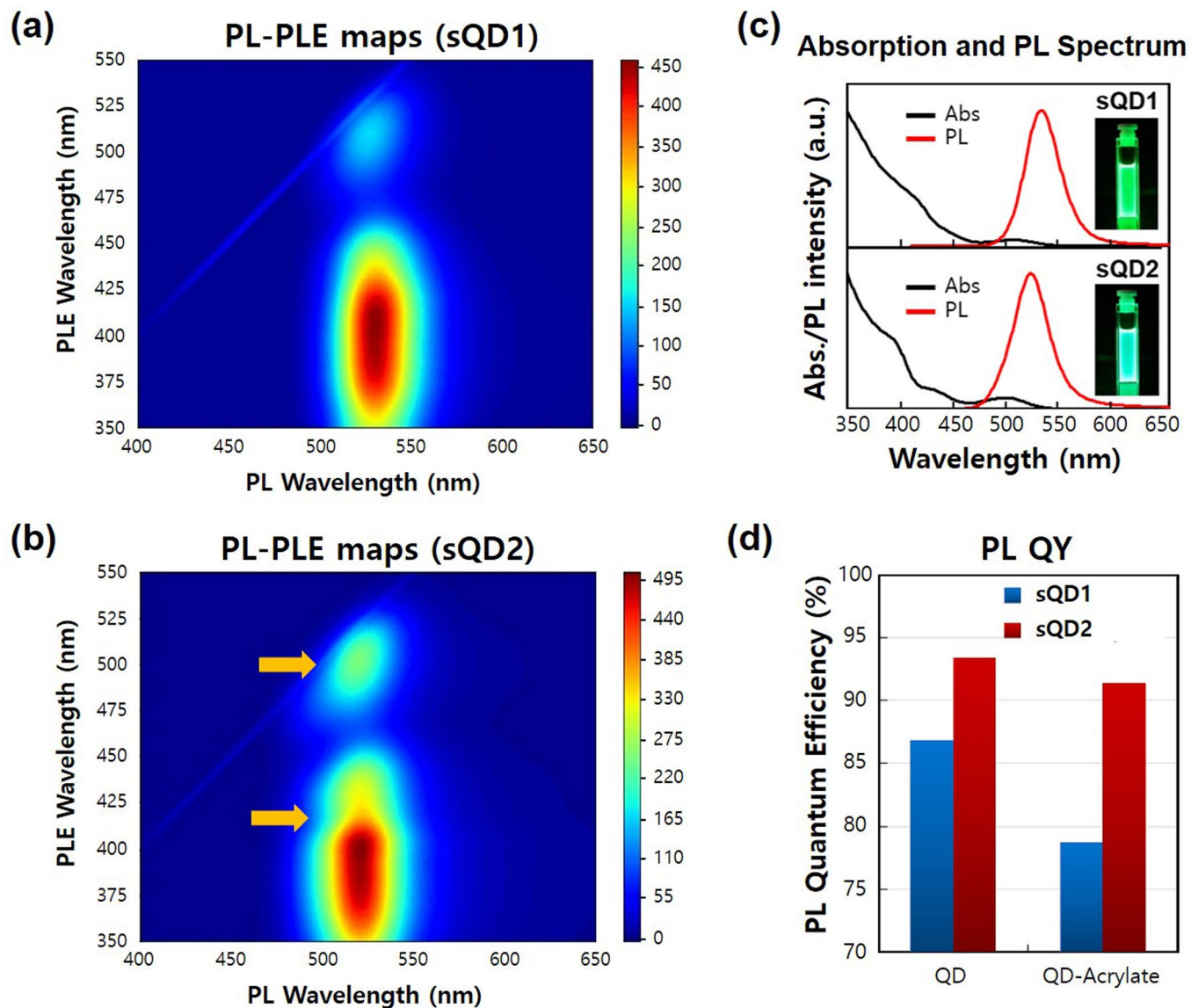
Extended Data Fig. 3 | Conventional EDX images of sQD1 and sQD2. (a) sQD1 and (b) sQD2 images acquired using Titan Cubed TEM 60-300 at 300kV, 8 μ s dwell time. Se, S, and Zn refer selenium, sulphur, and zinc components, respectively.



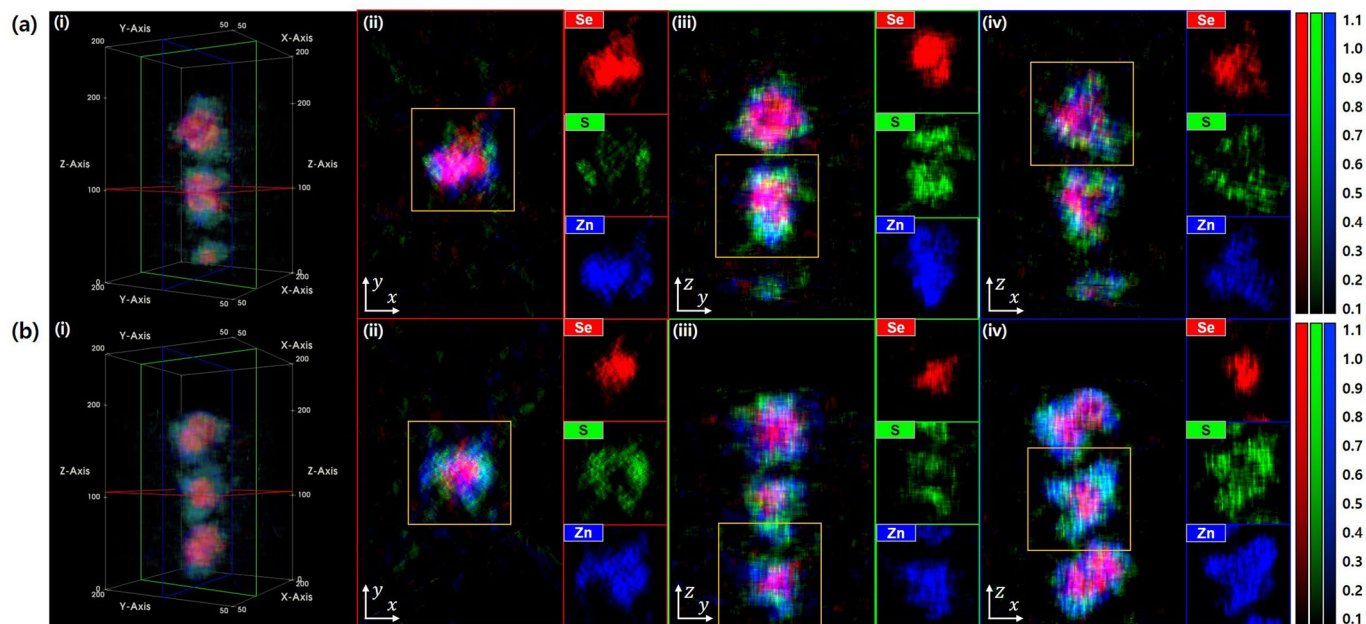
Numerical average		Gaussian fitting		AR	Solidity
Mean	SD	Center	Width		
8.9892	1.4534	8.8663	3.0740	1.25	0.85

Numerical average		Gaussian fitting		AR	Solidity
Mean	SD	Center	Width		
9.0194	0.6030	9.0305	1.1531	1.27	0.87

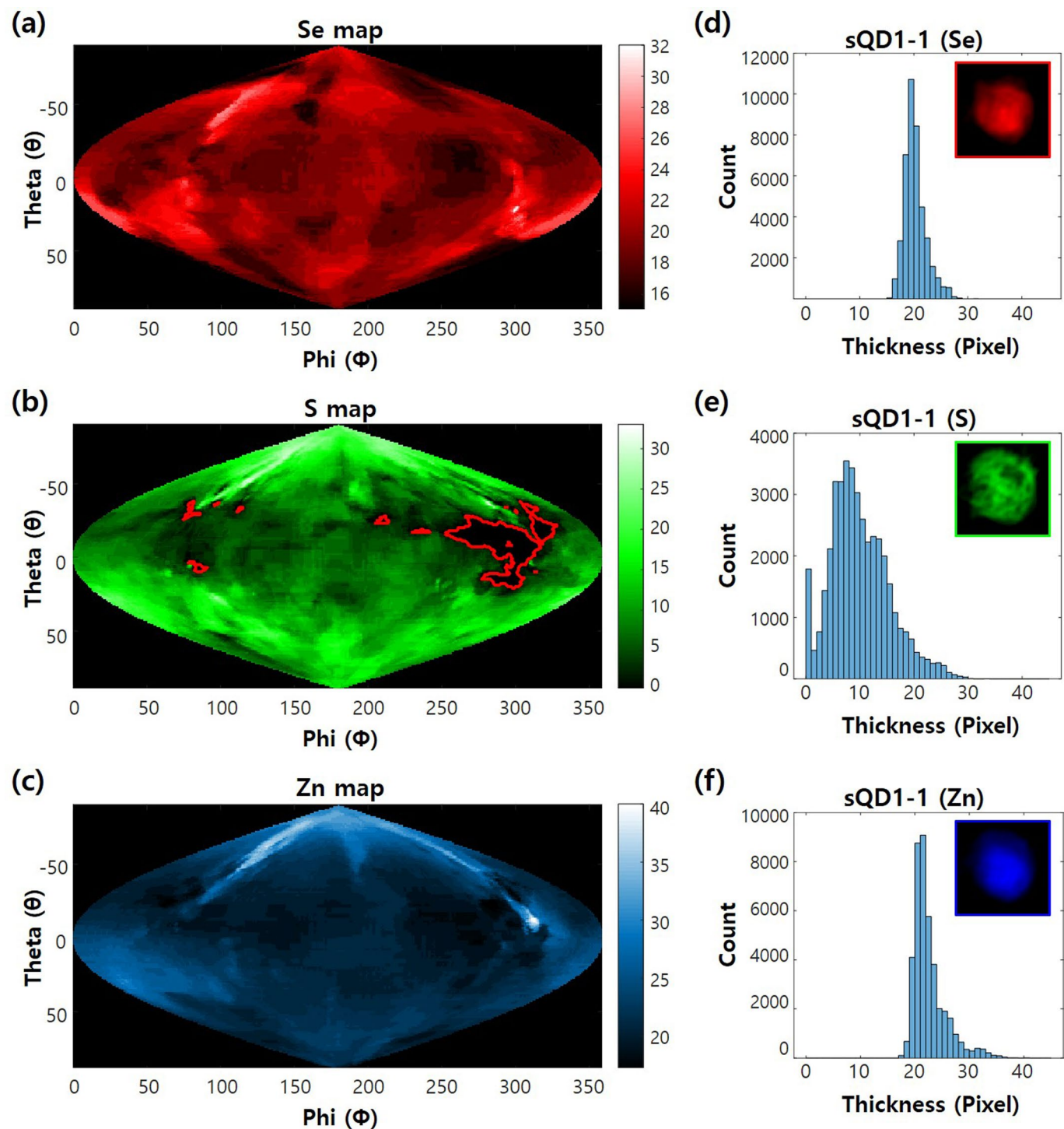
Extended Data Fig. 4 | Conventional method for analysing QD shape information in TEM images. sQD images were acquired using Titan Cubed TEM 60-300 at 300 kV, 8 μ s dwell time. Total number of particles are 338 and 264 for sQD1 and sQD2, respectively. The image analysis was done with Image J. To isolate particle and background, we calculate mean value of the total images to use as the threshold value. The diameter is calculated as equivalent circular area diameter using the number of counted pixels on each particle.



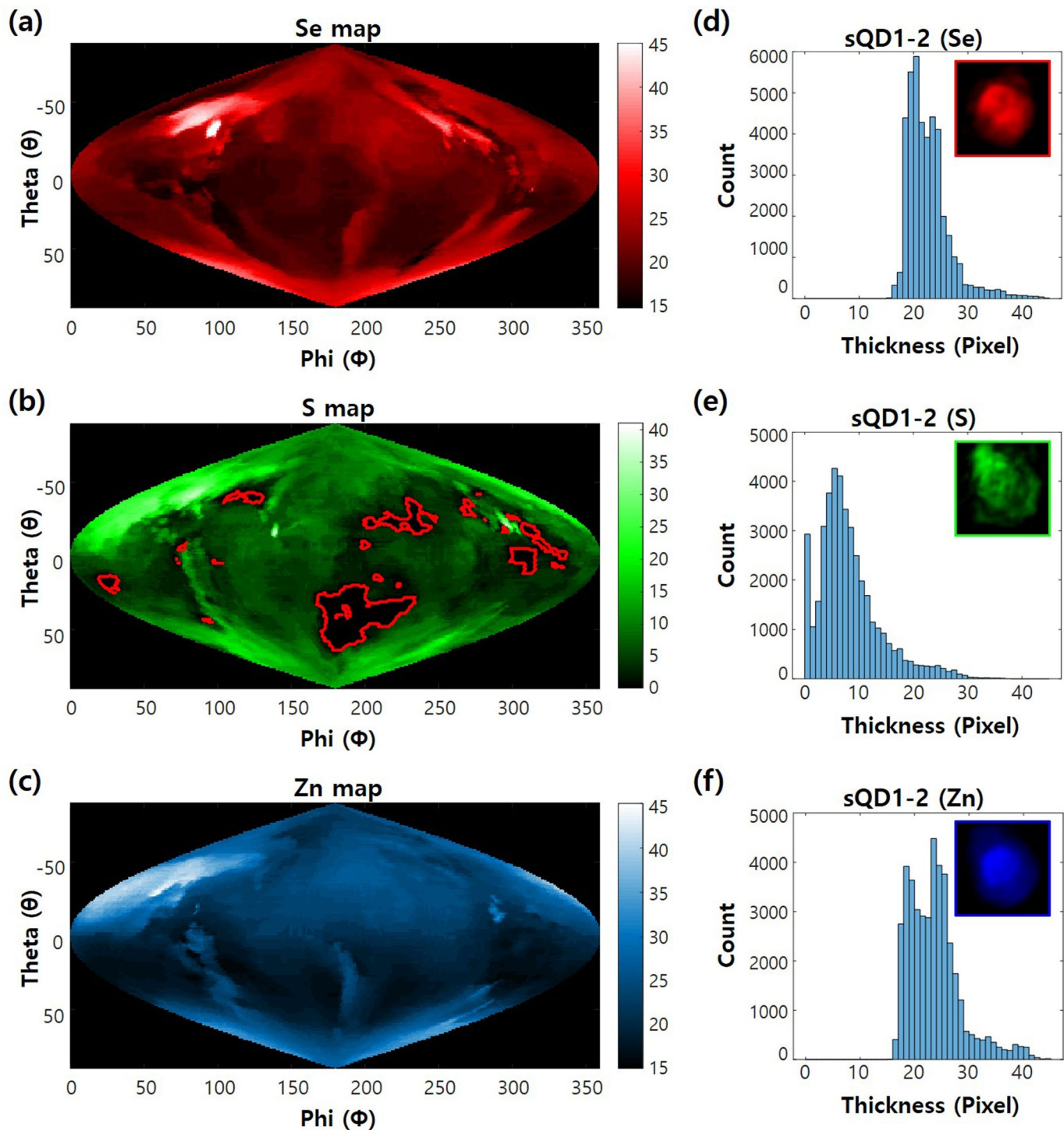
Extended Data Fig. 5 | Photoluminescence characteristics of sQD1 and sQD2. (a) and (b) are PL-PLE maps of sQD1 and sQD2 dispersed in toluene. Yellow arrows indicate the characteristic points of sQD2 compared sQD1. (c) Absorption and PL spectra for sQD1 and sQD2. (d) Comparison of their quantum efficiency.



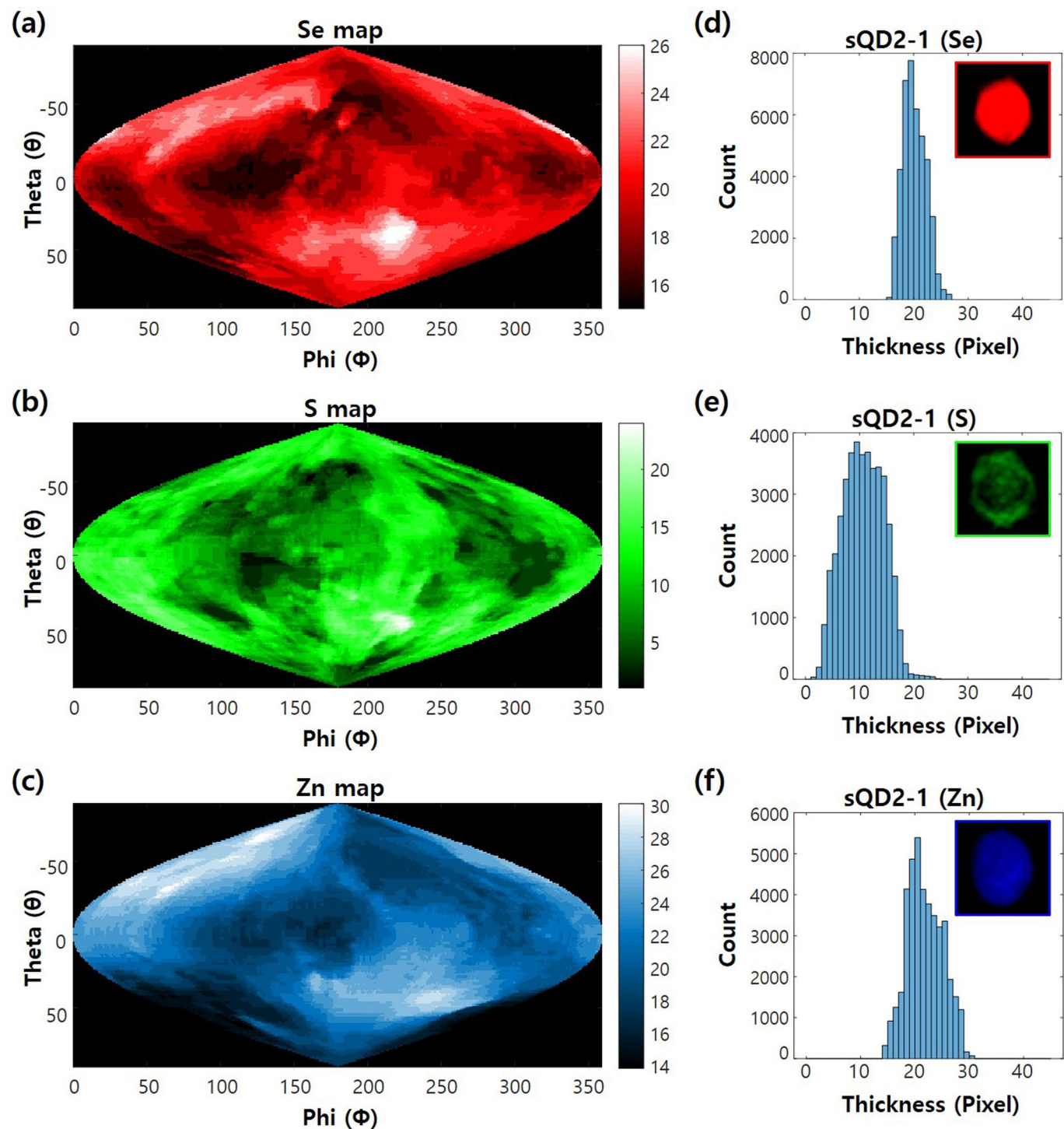
Extended Data Fig. 6 | SIRT 3D STEM-EDX reconstruction results with spatial 11×11 average filter. (a) and (b) show the reconstruction results using sQD1 and sQD2, respectively. (i) shows the 3D rendering results, and red, green, and blue boxes in (i) indicate (ii) xy-, (iii) yz-, and (iv) xz-plane cut-view, respectively. Yellow boxes illustrate the magnified images. Se, S, and Zn refer selenium, sulphur, and zinc components, respectively.



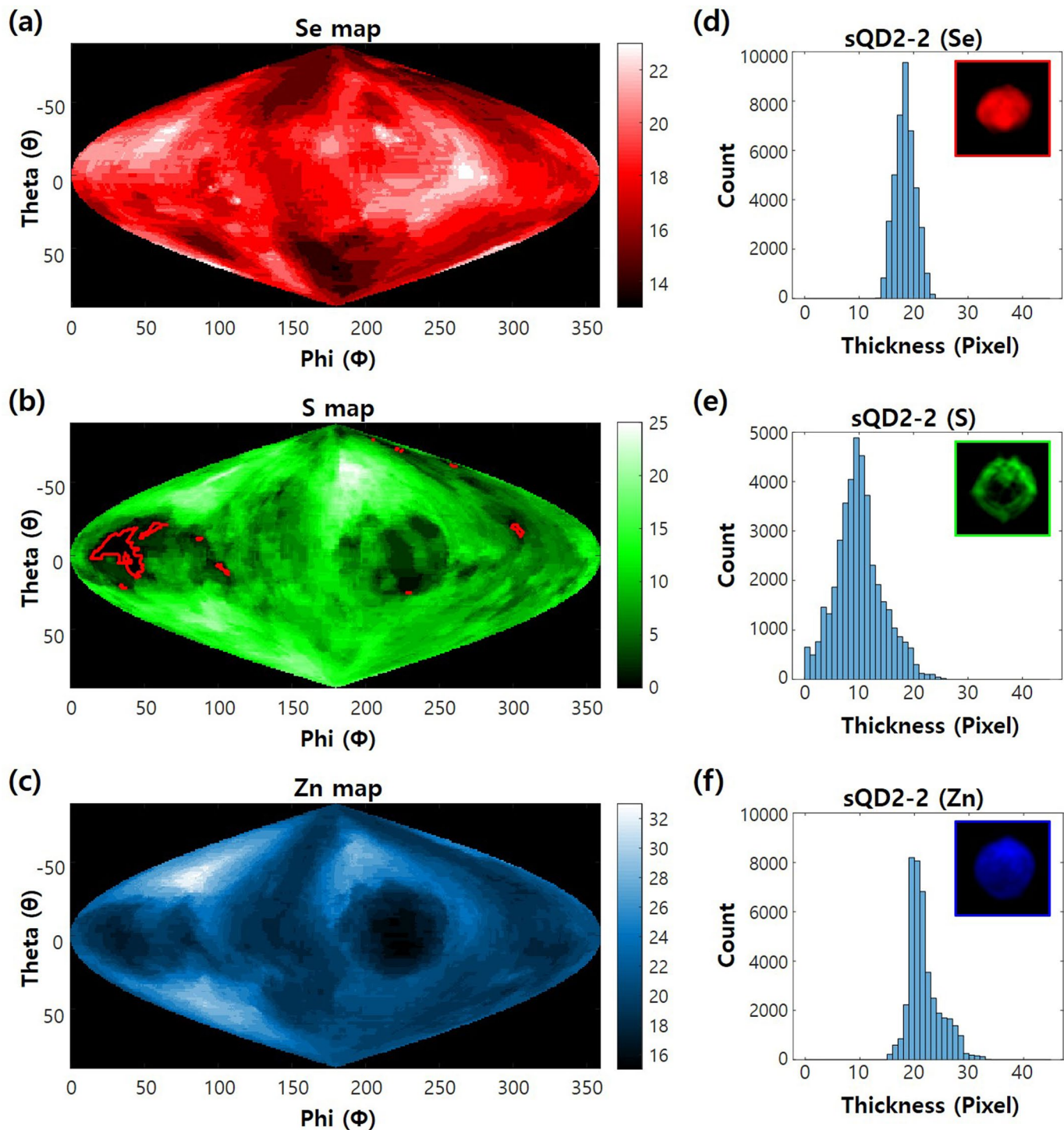
Extended Data Fig. 7 | sQD1-1 thickness maps on spherical coordinates Φ and θ . (a-c) sQD1-1 particle 2-D transformed element images; Red, green, and blue represent Se, S, and Zn, respectively. Se, S, and Zn thickness maps at $0^\circ \leq \Phi < 360^\circ$ and $-90^\circ \leq \theta \leq 90^\circ$. (d-f) Histogram of Se, S, and Zn thickness maps. Insets are projection images of Se, S, and Zn along z-axis. Colorbars are the number of accumulated pixels at each Φ and θ values.



Extended Data Fig. 8 | sQD1-2 thickness maps on spherical coordinate Φ and θ . (a-c) sQD1-2 particle 2-D transformed element images; Red, green, and blue represent Se, S, and Zn, respectively. Se, S, and Zn thickness maps at $0^\circ \leq \Phi < 360^\circ$ and $-90^\circ \leq \theta \leq 90^\circ$. (d-f) Histogram of Se, S, and Zn thickness maps. Insets are projection images of Se, S, and Zn along z-axis. Colorbars are the number of accumulated pixels at each Φ and θ values.



Extended Data Fig. 9 | sQD2-1 thickness maps on spherical coordinate Φ and θ . (a-c) sQD2-1 particle 2-D transformed element images; Red, green, and blue represent Se, S, and Zn, respectively. Se, S, and Zn thickness maps at $0^\circ \leq \Phi < 360^\circ$ and $-90^\circ \leq \theta \leq 90^\circ$. (d-f) Histogram of Se, S, and Zn thickness maps. Insets are projection images of Se, S, and Zn along z-axis. Colorbars are the number of accumulated pixels at each Φ and θ values.



Extended Data Fig. 10 | sQD2-2 thickness maps on spherical coordinate Φ and θ . (a-c) sQD2-2 particle 2-D transformed element images; Red, green, and blue represent Se, S, and Zn, respectively. Se, S, and Zn thickness maps at $0^\circ \leq \Phi < 360^\circ$ and $-90^\circ \leq \theta \leq 90^\circ$. (d-f) Histogram of Se, S, and Zn thickness maps. Insets are projection images of Se, S, and Zn along z-axis. Colorbars are the number of accumulated pixels at each Φ and θ values.